Multi-frequency Integration Algorithm of Contrast Source Inversion Method for Microwave Breast Tumor Detection*

Hiroki Sato[1] and Shouhei Kidera[1]

Abstract— Microwave mammography is one of the most promising alternatives to X-ray-based breast cancer detection techniques, where a malignant tumor has a certain level of dielectric property contrast compared with those in normal tissues. However, the inverse problem of reconstructing complex permittivity is a non-linear and ill-posed problem, and the appropriate selection of such algorithms is the key to the success of microwave mammography. The contrast source inversion (CSI) method is the most promising solution to the above problem, where the iterative procedure does not require a computationally expensive forward solver, like the finite difference time domain (FDTD) method. However, the conventional CSI method assumes a non-dispersive dielectric model, while breast or other human tissues have a non-negligible dispersive property. To address this problem, this paper introduces an extended CSI method, which is suitable for dispersive medium and in which multi-frequency integration is introduced to enhance the reconstruction accuracy. The FDTD numerical test, which uses a realistic breast phantom via magnetic resonance imaging (MRI), demonstrates that our proposed method efficiently enhances the reconstruction accuracy even in dispersive medium.

I. INTRODUCTION

Recent reports from the World Cancer Research Fund have revealed that breast cancer has become one of the most widely diagnosed cancers in women [1]. Microwave-based breast cancer detection, known as microwave mammography, is one of the promising options for frequent screening for cancer, which may be used as an alternative to the traditional X-ray mammography, ultrasound, and magnetic resonance imaging (MRI) in terms of cost, compactness, and safety. While X-ray mammography is the most commonly used imaging modality, it has a serious risk because of X-ray exposure to normal cells [2]. Ultrasound imaging has some advantages in terms of cost, portability, and suitability, especially for women with dense breasts [3]. The MRI-based modality has disadvantages in terms of its high cost and the large equipment required [4].

Microwave mammography is based on the clinical fact that there is a significant dielectric property contrast between normal and malignant tissue in breasts at microwave frequencies. M. Lazebnik et al. demonstrated that there is a significant dielectric property contrast between normal and malignant tissue when measuring excised breast tissue specimens [5]. J. D. Shea et al. also revealed that the dispersion property

and fitting parameters using the single-pole Debye model [4] for the complex permittivity of breast tissue are from 0.5 to 3.5 GHz [6]. Microwave imaging algorithms are mainly divided into two categories: the radar-based approach and the tomographic approach. Studies have shown that [7] the space-time beamforming-based radar approach has successfully demonstrated its effectiveness by processing a number of tumor reflections. However, this method suffers from a lower contrast image when the malignant tumor is buried in the fibroglandular tissue, which has the same level of dielectric property as cancer.

In contrast, the tomographic approach is considered more promising because a complex dielectric map can be reconstructed by solving the domain integral equation. However, the above integral equation cannot be solved easily because it is non-linear and an ill-posed problem. In particular, conventional Born approximation-based methods, such as diffraction tomography [8], suffer from inaccuracy in dealing with the dielectric property map that has a much higher contrast than the background medium. Among the numerous inverse scattering algorithms, the distorted Born iterative method (DBIM) is one of the most promising algorithms because it updates the background profile to maintain the linearity of the problem. Some literature has shown that the DBIM offers accurate results even for dispersive breast medium, including cancer [9], [10], [11]. However, the DBIM basically requires a forward solver in each iterative step, and it would take an enormous amount of computation, especially for dealing with a three-dimensional problem.

Considering this background, we focused on the contrast source inversion (CSI) method [12], which also solves the non-linear integral equation by iteration steps. However, the CSI does not require a computationally expensive forward solver, such as FDTD; instead, it simultaneously solves the state and data equation. In addition, a multiple frequency strategy for the CSI method, such as frequency hopping, was developed for accuracy enhancement in refs. [13], [14]. However, there are very few studies that have focused on the CSI method and that dealt with a frequency-dependent dielectric object, such as breasts or other human tissues.

To address this problem, this paper introduces a multi-frequency integration scheme for the CSI method for dispersive breast medium [13]. This method first reconstructs the complex permittivity map for each frequency using the traditional CSI method, and the frequency-dependent characteristic is sequentially determined by the single-pole Debye model. In addition, this method integrates the multi-frequency CSI outputs by considering the Debye curve using

the differentiation of the Debye formula. Two-dimensional (2-D) FDTD numerical tests that use the MRI-derived realistic breast phantom demonstrated that our proposed method efficiently enhances the reconstruction accuracy even for a dispersive model.

II. OBSERVARTION MODEL

Figure 1 shows the observation model for breast cancer detection using microwaves. The breast medium is comprised of skin, adipose, fibro-glandular, and tumor tissues, each of which has a lossy, dispersive, and isotropic dielectric property. A number of arrays of transmitting and receiving antennas form the cylindrical array surrounding the breast, the region of which denotes S. Microwave signals are sequentially sent from each transmitting antenna and then recorded at all receiving antennas. The locations of the transmitting and receiving antennas are denoted as r_t and r_r, respectively. $E^{\text{total}}(r_t, r_r; t)$ denotes the total electric field for each antenna combination.

Fig. 1: Observation model.

III. CSI METHOD

A. Forward Problem Formulation

In assuming the scatter in the domain $r \in D$, the electric scattered field is expressed using the Helmholtz type domain integral equation as

$$E^{\text{scat}}(r_t, r_r, \omega) \equiv E^{\text{total}}(r_t, r_r, \omega) - E^{\text{in}}(r_t, r_r, \omega)$$
$$= k_b^2 \int_D G_b(r_r, r, \omega)\chi(r, \omega)E^{\text{total}}(r_t, r, \omega)dr, r \in D, \quad (1)$$

where $E^{\text{total}}(r_t, r_r, \omega)$ is the total field, $E^{\text{in}}(r_t, r_r, \omega)$ is the incident field, k_b is the wavenumber for the background, μ is the permeability, $G_b(r_r, r, \omega)$ is Green's function of the background, and $\chi(r, \omega) \equiv \varepsilon(r, \omega)/\varepsilon_b(r, \omega) - 1$. The Green's function is calculated as

$$G_b(r_r, r, \omega) = -(j/4)H_0^{(2)}(k_b|r_r - r|), \quad (2)$$

where $H_0^{(2)}$ is the zero-order Hankel function of the second kind. Here the CSI algorithm introduces a dummy variable, the so-called contrast source as

$$w(r, \omega) \equiv E^{\text{total}}(r_t, r, \omega)\chi(r, \omega). \quad (3)$$

Then, Eq. (1) is reformed as

$$E^{\text{scat}}(r_t, r_r, \omega) = k_b^2 \int_D G_b(r_r, r, \omega)w(r, \omega)dr, (r \in D). \quad (4)$$

Here, the contrast source is

$$w(r, \omega) = \chi(r, \omega)E^{\text{in}}(r_t, r', \omega)$$
$$+ \chi(r, \omega)k_b^2 \int_D G_b(r', r, \omega)w(r, \omega)dr, r, (r \in D), \quad (5)$$

where subscripts S and D indicate the domain of the array and scatterer, respectively, as shown in Fig. 1. Here, we introduce the notations for the integrals in Eqs. (4) and (5) as

$$G_S w(r, \omega) = k_b^2 \int_D G_b(r_r, r, \omega)w(r, \omega)dr, (r \in D), \quad (6)$$

$$G_D w(r, \omega) = k_b^2 \int_D G_b(r', r, \omega)w(r, \omega)dr, (r' \in D). \quad (7)$$
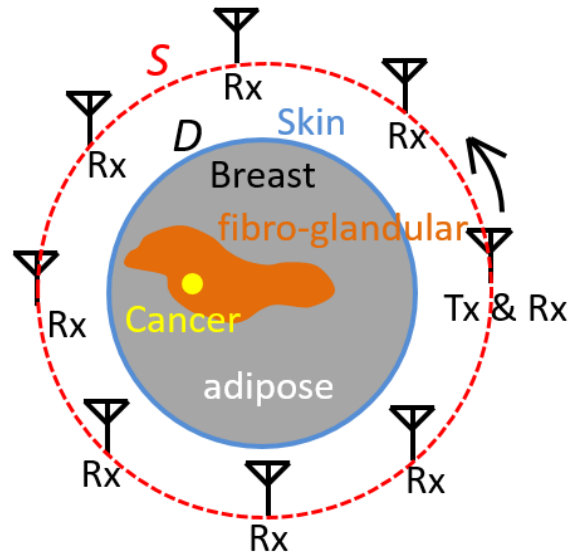
Here, Eq. (6) is named the data equation, and Eq. (7) is called the state (or object) equation.

B. Inversion Algorithm

To extract the contrast function $\chi(r, \omega)$, the CSI defines the following cost function:

$$F(\chi, w) \equiv \frac{\sum_{r_r \in S} \|E^{\text{scat}}(r_t, r_r, \omega) - G_j^S w(r, \omega)\|_S^2}{\sum_{r_r \in S} \|E^{\text{scat}}(r_t, r_r, \omega)\|_S^2}$$
$$+ \frac{\sum_{r' \in D} \|\chi(r, \omega)E^{\text{in}}(r_t, r', \omega) - w(r, \omega) + \chi(r, \omega)G_j^D w(r, \omega)\|_D^2}{\sum_{r' \in D} \|\chi(r, \omega)E^{\text{in}}(r_t, r', \omega)\|_D^2}, \quad (8)$$

where $\|\cdot\|_S^2$ and $\|\cdot\|_D^2$ are the l_2 norms defined as the S and D domains, respectively. Of note, the first and second terms are the errors from data equation (4) and state equation (5), respectively. The cost function $F(\chi, w)$ is minimized by sequentially updating the valuables as $w(r, \omega)$, $E^{\text{total}}(r_t, r, \omega)$, and $\chi(r, \omega)$.

IV. MULTI-FREQUENCY INTEGRATED CSI

Some studies have revealed that the multiple frequency strategy for the CSI method may enhance the reconstruction accuracy, such as a frequency hopping scheme [13], [14]. However, the traditional multi-frequency CSI does not deal with dispersive media or objects, and there have been quite a few reports that have applied such methods to the dispersive breast tumor detection scenario. In those traditional methods, they considered the frequency dependency for only the imaginary part of the relative complex permittivity, which is formulated as follows,

$$\varepsilon_r(\omega; \varepsilon_\infty, \sigma_s) = \varepsilon_\infty + \frac{\sigma_s}{j\omega\varepsilon_0}, \quad (9)$$

where ε_∞ denotes the relative permittivity at the infinite frequency, and σ_s denotes the conductivity. However, many

studies have demonstrated that all tissues in the breast can be well modeled by the single-pole Debye model as, [4]

$$\varepsilon_{\text{Debye}}(\omega; \varepsilon_\infty, \Delta\varepsilon, \sigma_s) = \varepsilon_\infty + \frac{\Delta\varepsilon}{1+j\omega\tau} + \frac{\sigma_s}{j\omega\varepsilon_0}, \quad (10)$$

where $\Delta\varepsilon$ is the difference between ε_∞ and the relative permittivity at zero frequency, and τ denotes the relaxation time. To achieve an appropriate integration for the multi-frequency CSI results, the above frequency dependency should be considered in our proposed method.

To implement the above algorithm, the proposed method initially estimates the Debye parameters from the multiple CSI results in each frequency. Then, the least square mini-mization is introduced to estimate the Debye parameters as,

$$(\hat{\varepsilon}_\infty, \Delta\hat{\varepsilon}, \hat{\sigma}_s) = \arg\min_{(\varepsilon_\infty, \Delta\varepsilon, \sigma_s)} \sum_{i=1}^{N_f} |\varepsilon_{\text{Debye}}(f_i; \varepsilon_\infty, \Delta\varepsilon, \sigma_s) - \tilde{\varepsilon}^{\text{init}}(f_i)|^2,$$
$$(11)$$

where $\tilde{\varepsilon}^{\text{init}}(f_i)$ denotes the initial estimate of the CSI for each frequency f_i, and N_f denotes the total number of multiple frequencies in the integration. We focus on the CSI result at a specific frequency f_i, and this result is compensated by using other all frequencies as follows:

$$\hat{\varepsilon}(f_i) = \frac{\sum_{j=1}^{N_f} \exp\left(\frac{-(f_i-f_j)^2}{2\sigma_f^2}\right) \tilde{\varepsilon}(f_i; f_j)}{\sum_{j=1}^{N_f} \exp\left(\frac{-(f_i-f_j)^2}{2\sigma_f^2}\right)}, \quad (12)$$

where $\tilde{\varepsilon}(f_i; f_j)$ is modeled as the first order approximation;

$$\tilde{\varepsilon}(f_i; f_j) \equiv \hat{\varepsilon}(f_j) + \left.\frac{d\varepsilon_r}{df}\right|_{f=f_j} (f_i - f_j), \quad (13)$$

where $\frac{d\varepsilon_r}{df}$ is defined as the differentiation of the right term in Eq. (10) with respect to f as,

$$\frac{d\varepsilon_r}{df} \equiv -\frac{j2\pi\tau\Delta\hat{\varepsilon}}{(1+j2\pi f\tau)^2} - \frac{\hat{\sigma}_s}{j2\pi f^2\varepsilon_0}. \quad (14)$$

This method can appropriately integrate the multi-frequency CSI results for the specific frequency, and may enhance the reconstruction accuracy compared with that obtained by the single frequency CSI result.

V. NUMERICAL SIMULATION

This section describes the 2-D FDTD-based numerical tests using a realistic numerical breast phantom of healthy women [15]: a data set of the Class 3 (heterogeneously dense) phantom is assumed, where a $z = 16$ mm slice is investigated. Here, Fig. 2 shows the original relative complex permittivity of the breast phantom at the center frequency, including the cancer cells with a 6-mm size and the Debye parameter as $(\varepsilon_\infty, \Delta\varepsilon, \sigma_s) = (18.0, 31.0, \text{and } 0.75 \text{ S/m})$ [10]. The source current forms a raised-cosine pulse with a 2.0-GHz center frequency and a 2.1-GHz bandwidth. The array with 30 antennas is arranged as the area surrounding the breast, where each antenna sequentially transmits and receives signals; specifically, the data for all combinations
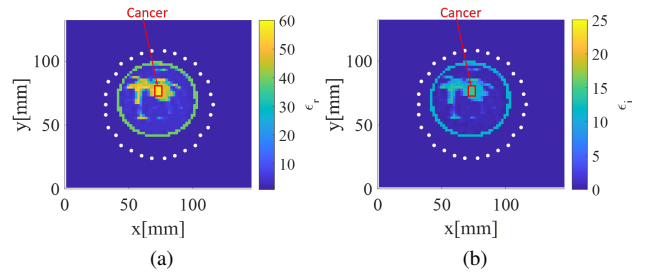
Fig. 2: 2-D numerical breast phantom (Class 3) and configuration. The hollow circle denotes the location of the transmitting and receiving antenna. The colorbar displays (a): the real and (b): the imaginary parts of complex permittivity.

(a) $f = 1.44$ GHz   (b) $f = 1.55$ GHz   (c) $f = 1.67$ GHz

(d) $f = 1.78$ GHz   (e) $f = 1.90$ GHz   (f) $f = 2.01$ GHz

(g) $f = 2.13$ GHz   (h) $f = 2.24$ GHz   (i) $f = 2.36$ GHz
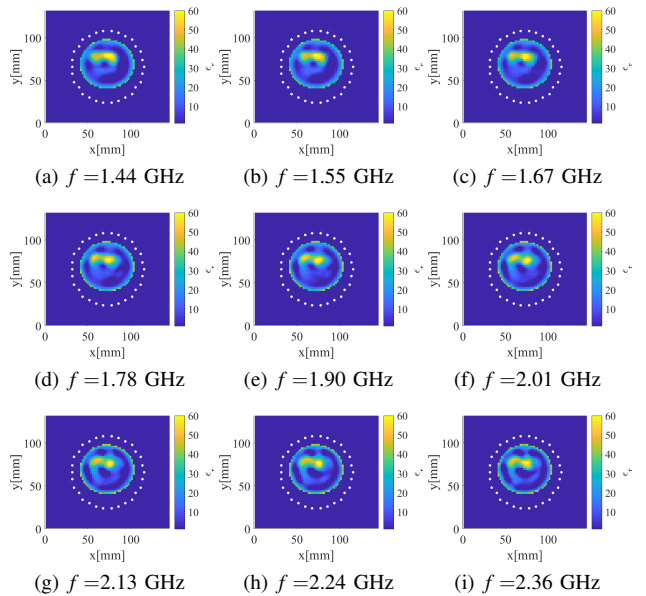
Fig. 3: Reconstruction results of the CSI for each frequency for real part of complex permittivity.

of transmitting and receiving antennas are processed in the CSI. The scattered electric field is calculated by the FDTD method, assuming the single-pole Debye model. Both the size of the FDTD and the unknown pixel are 2 mm. The noiseless case is assumed. We investigated multiple frequen-cies from 1.44 GHz to 2.53 GHz with a 0.0575-GHz sample, which is defined as Δf, resulting in 20 frequency samples. The CSI calculation was performed at each frequency, and the number of iterations for the CSI was 30000. Figures 3 and 4 show the initial estimates using the CSI method for each frequency. The average computational time for each frequency CSI was approximately 1200 s using an Intel(R) Xeon(R) CPU E5-2620 with 2.4 GHz and 128 GB RAM. As shown in these figures, there are differences among the results obtained at multiple frequencies, and we need to consider the appropriate integration scheme for these results while also considering the frequency dependency. Figure 5 also shows the results of the single-pole Debye fitting using the multiple frequency CSI results, at specific pixels. Figure 6 compares the results for the single frequency CSI and the

(a) $f = 1.44$ GHz (b) $f = 1.55$ GHz (c) $f = 1.67$ GHz

(d) $f = 1.78$ GHz (e) $f = 1.90$ GHz (f) $f = 2.01$ GHz

(g) $f = 2.13$ GHz (h) $f = 2.24$ GHz (i) $f = 2.36$ GHz
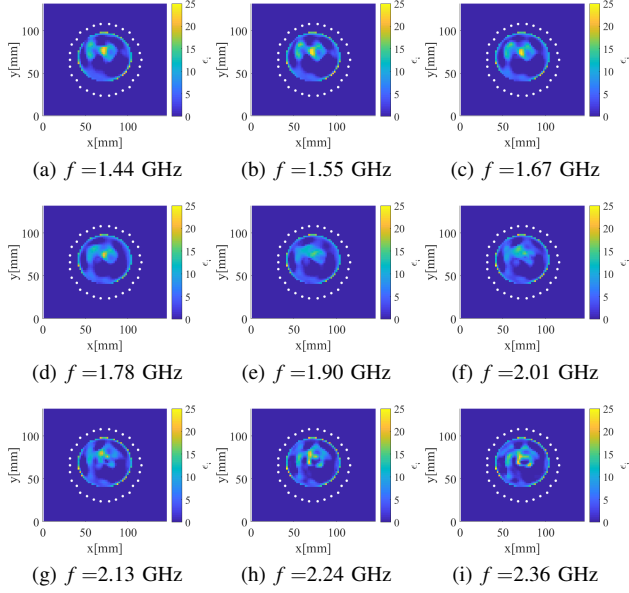
Fig. 4: Reconstruction results of the CSI for each frequency for imaginary part of complex permittivity.

(a)   (b)
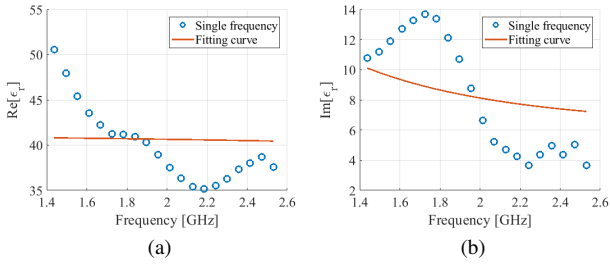
Fig. 5: Estimations of complex permittivity ((a): real and (b): imaginary parts) and fitting curve based on the single pole Debye model.

proposed multi-frequency integrated CSI at the frequency of 2.01 GHz, where the two parameters σ_f in the proposed method were investigated. Here, the normalized root mean square error (NRMSE) for the real and imaginary complex permittivity is introduced for the quantitative error analysis as,

$$\text{NRMSE}_{\varepsilon_r'} = \sqrt{\frac{1}{K}\sum_{k=1}^{K}\left|\frac{\varepsilon_r'(\boldsymbol{r}_k) - \varepsilon_{r,\text{true}}'(\boldsymbol{r}_k)}{\bar{\varepsilon}_{r,\text{max}}'}\right|^2}, \quad (15)$$

$$\text{NRMSE}_{\varepsilon_r''} = \sqrt{\frac{1}{K}\sum_{k=1}^{K}\left|\frac{\varepsilon_r''(\boldsymbol{r}_k) - \varepsilon_{r,\text{true}}''(\boldsymbol{r}_k)}{\bar{\varepsilon}_{r,\text{max}}''}\right|^2}, \quad (16)$$

where ε_r' and ε_r'' are the real and imaginary parts of the complex permittivity, respectively; the subscript "true" denotes the original value, the subscript "max" denotes the max value, and K denotes the number of cells in the ROI. Table 1 shows the NRMSE for each results. Figure 7 compares the histogram of errors for both the real and imaginary parts of the complex permittivity for all pixels of the ROI area for the single frequency CSI and for the proposed method. Table 2 shows the cumulative probabilities of the reconstruction

(a)   (b)

(c)   (d)

(e)   (f)
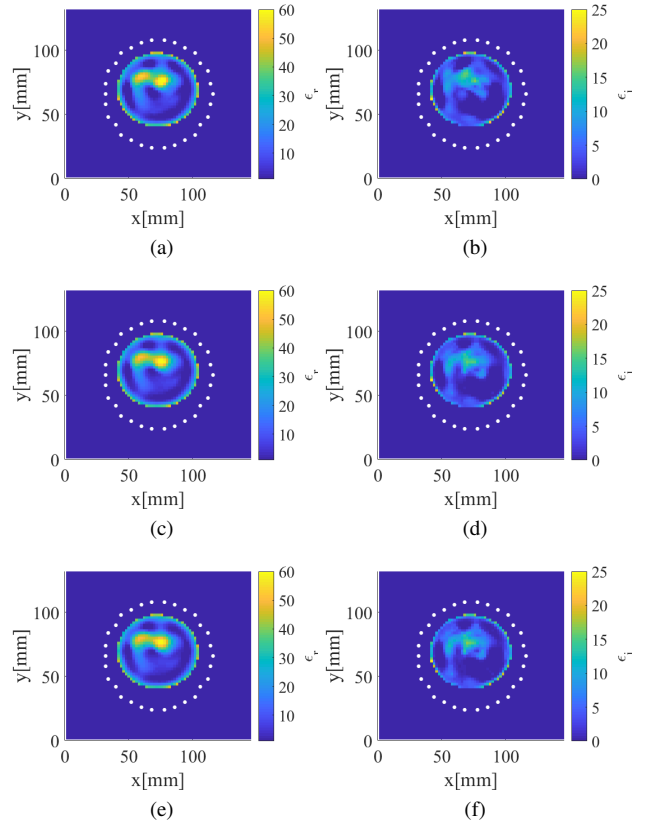
Fig. 6: Results of complex permittivity reconstruction: (a) and (b): using the single frequency CSI. (c) and (d): using the proposed method with $\sigma_f = 5\Delta f$. (e) and (f): using the proposed method with $\sigma_f = 10\Delta f$.

TABLE I: Results of NRMSE at the frequency 2.01 GHz.

	Re$[\varepsilon_r]$	Im$[\varepsilon_r]$
Single frequency (Namely, $\sigma_f = 0$)	0.1688	0.2497
$\sigma_f = 5\Delta f$	0.1662	0.2348
$\sigma_f = 10\Delta f$	0.1663	0.2336

errors for each method. As shown in this table, the proposed method significantly increased the number of pixels with a high accuracy.

VI. CONCLUSIONS

We presented a multi-frequency integration-based CSI method for dispersive breast medium that combines multiple frequency results using the Debye formula. Numerical simulation combined with realistic breast phantoms offers a subtle enhancement in the NRMSE compared with single frequency results. Additionally, the histogram of errors for both the real and imaginary parts of the complex permittivity indicates an improvement in the reconstruction accuracy of the complex permittivity by integrating the multi-frequency data.

(a) $\sigma_f = 5\Delta f$ (b) $\sigma_f = 5\Delta f$

(c) $\sigma_f = 10\Delta f$ (d) $\sigma_f = 10\Delta f$
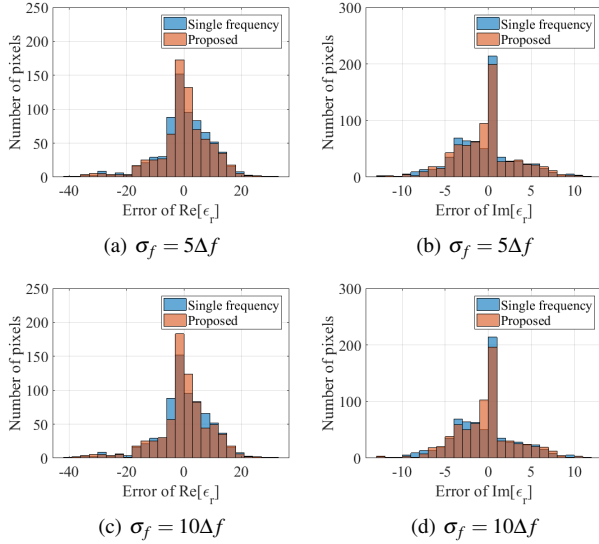
Fig. 7: Error distribution. (a) and (b): Case of $\sigma_f = 5\Delta f$. (c) and (d): Case of $\sigma_f = 10\Delta f$.

TABLE II: Cumulative probabilities for each method.

	Error of Re$[\varepsilon_r]$ ≤ 5	Error of Im$[\varepsilon_r]$ ≤ 2
Single frequency ($\sigma_f = 0$)	52.8%	49.7%
Proposed ($\sigma_f = 5\Delta f$)	55.4%	52.6%
Proposed ($\sigma_f = 10\Delta f$)	55.9%	53.6%

REFERENCES

[1] F. Bray, J. Ferlay, I. Soerjomataram, et al., "Global cancer statistics 2018: GLOBOCAN estimates of incidence and mortality worldwide for 36 cancers in 185 countries", *Cancer Jnl. for Clinicians*, vol. 68, no. 6, pp. 394?424, Dec., 2018.

[2] S. Goto, Y. Azuma, T. Sumimoto, T. Maruyama, and S. Eiho, "Measurement of Patient Exposure Dose on X-Ray Screening Mammography", *IEEE Instrumantation and Measurement Technology Conference*, pp. 191-196, May, 2001.

[3] G. A. G. M. Hendriks, C. Chen, H. H. G. Hansen, and C. L. de Korte,"3-D Single Breath-Hold Shear Strain Estimation for Improved Breast Lesion Detection and Classification in Automated Volumetric Ultrasound Scanners ", *IEEE Transactions on Ultrasonics, Ferroelectrics, and Frequency Control*, Vol. 65, no. 9, pp. 1590-1599, Sept., 2018.

[4] J. D. Shea, P. Kosmas, S. C. Hagness, and B. D. Van Veen,"Three-dimensional microwave imaging of realistic numerical breast phantoms via a multiple-frequency inverse scattering technique", *Am. Assoc. Phys. Med.*, vol. 37, no. 8, pp. 4210-4226, Aug., 2010.

[5] M. Lazebnik, at al.,"A large-scale study of the ultrawideband microwave dielectric properties of normal, benign and malignant breast tissues obtained from cancer surgeries", *IOP Publishing Ltd*, pp. 6093-6115, 2007.

[6] J. D. Shea, P. Kosmas, B. D. Van Veen, and S. C. Hagness,"Contrast-enhanced microwave imaging of breast tumors: a computational study using 3-D realistic numerical phantoms", *Inverse Probl.*, 2010.

[7] E. J. Bond, et al.,"Microwave imaging via space-time beamforming for early detection of breast cancer," *IEEE Trans: Antennas Propagat:*, vol. 1, no. 8, pp. 1690-1705, Aug. 2003.

[8] P. Muller, M. Schurmann, and J. Guck,"The Theory of Diffraction Tomography", Oct., 2016.

[9] D. W. Winters, B. D. Van Veen, and S. C. Hagness,"A Sparsity Regularization Approach to the Electromagnetic Inverse Scattering Problem", *IEEE Trans: Antennas Propagat:*, vol. 58, no. 1, pp. 145-154, Jan., 2010.

[10] F. Gao, B. D. Van Veen, and S. C. Hagness,"Sensitivity of the Distorted Born Iterative Method to the Initial Guess in Microwave Breast Imaging", *IEEE Trans: Antennas Propagat:*, vol. 63, no. 8, pp. 145-154, Aug., 2015.

[11] M. Azghani and F. Marvasti,"L_2-Regularized Iterative Weighted Algorithm for Inverse Scattering", *IEEE Trans. Antennas Propaga.*, vol. 64, no. 6, pp. 2293-2300, June, 2016.

[12] P. M. van den Berg and A. Abubakar,"Contarast Source Inversion Method: State of Art", *Progress In Electromagnetics Research, PIER 34*, pp. 189-218, 2001.

[13] S. Sun, B. J. Kooij, T. Jin and A. Yarovoy,"Through-wall Imaging by TE and TM Hybrid Polarization Inversion Based on FDFD and Frequency Hopping Scheme", *IET International Radar Conference 2015*, Apr., 2016.

[14] S. Sun, B. J. Kooij, T. Jin and A. Yarovoy,"Simultaneous Multi-Frequency TE/TM Polarization Inversion Based on FDFD for Ground Penetrating Radar", *2015 8th International Workshop on Advanced Ground Penetrating Radar (IWAGPR)*, July, 2015.

[15] UWCEM, "Numerical breast phantom repository", URL:https://uwcem.ece.wisc.edu/phantomRepository.html.